DOI: 10.26599/FSHW.2025.9250823

Contents lists available at SciOpen

Food Science and Human Wellness

journal homepage: https://www.sciopen.com/journal/2097-0765

China Food Publishing Co.

Multienzyme-like nanozymes-powered smartphone biosensor for on-site multicolor visual detection of aminoglycosides

Chunyan Sun[a,b*], Wenyi Yang[a], Jing Zhang[c], Huan Wang[a], Hongru Zheng[c], Zheng Liu[a], Junyang Wang[a], Xiangning Li[d], Rui Jin[a*]

[a] *Department of Food Quality and Safety, College of Food Science and Engineering, Jilin University, Changchun 130062, PR China*

[b] *Chongqing Research Institute, Jilin University, Chongqing, 401123, PR China*

[c] *Jilin Province Product Quality Supervision and Inspection Institute, Changchun, 130103, China*

[d] *School of Pharmacy, Beihua University, Jilin 132013, China*

ABSTRACT: Aminoglycosides (AGs) are widely used for the prevention and treatment of infectious diseases due to their bactericidal and bacteriostatic properties. However, the residues of AGs in milk have become a common concern in the food safety field due to the misuse of AGs, which has led to their over-accumulation in foods of animal origin. In this study, AGs regulate dual enzyme-mimicking activities (peroxidase-/catalase-like) of multienzyme nanozymes (AuNPs) were investigated, and the underlying activity regulation mechanisms were elucidated. In combination with the etching of gold nanorods (AuNRs), two multicolor visual biosensors were established using kanamycin (KAN) and tobramycin (TOB) as model analytes. Under neutral conditions, KAN enhanced the peroxidase-like activity of AuNPs and catalyzed the generation of more TMB^{2+}-etched AuNRs. Under alkaline conditions, TOB enhanced the catalase-like activity of AuNPs, reducing H_2O_2 residue and decreasing the extent of AuNRs etching. AuNRs served as signal transducers, exhibiting a linear correlation between their longitudinal surface plasmon resonance (LSPR) peak shift and AGs concentration. The distinct colorimetric changes accompanying the LSPR shift enabled the development of a multicolor visual sensing platform with enhanced visual discrimination. To enable portable analysis, smartphone technology was integrated into biosensors, achieving a low detection limit (0.464 nmol/L for KAN, 0.07 μmol/L for TOB) that is 100-fold lower than maximum residue limits. The biosensors demonstrate superior performance in the rapid, visual, and cost-effective detection of AGs in milk samples.

Keywords: Aminoglycosides, Nanozymes, AuNRs etching, Multicolor visual biosensor, Smartphone-based detection

1. Introduction

Aminoglycosides (AGs) are widely used to prevent and treat infectious diseases due to their bactericidal and bacteriostatic properties. The broad antimicrobial spectrum, low cost, and high sterilization efficiency of AGs, specifically kanamycin (KAN) and tobramycin (TOB), have made them highly recommended for combination therapy to support the healthy development of the livestock industry [1, 2]. However, overuse of these AGs can lead to contamination of animal-origin foods with antibiotic residues. These residues may accumulate in the food chain, when ingested in excess, cause toxic side effects in humans, including

***Corresponding author**
sunchuny@jlu.edu.cn (Chunyan Sun);
jinrui@jlu.edu.cn (Rui Jin)

Received 23 May 2025
Received in revised from 29 June 2025
Accepted 18 July 2025

ototoxicity, nephrotoxicity, neuromuscular blockade, hematopoietic toxicity, and allergic reactions [3, 4]. Furthermore, the misuse and overuse of AGs contribute to the emergence of antibiotic-resistant bacteria, which pose a serious threat to public health [5-7]. To mitigate these risks, many countries and regions have established maximum residue limits (MRLs) for AGs to ensure food safety. For instance, the European Union (EU) has set MRLs of 150 μg/kg for KAN and 200 μg/kg for TOB in milk [8].

Traditional methods for detecting AGs in food, such as gas chromatography (GC) and liquid chromatography-mass spectrometry (LC-MS), have the advantages of accuracy and reliability [9, 10]. However, their dependence on cumbersome instrumentation, intricate operational protocols, and prolonged sample pretreatment renders these methods impractical for real-time field applications requiring rapid on-site detection [11, 12]. In contrast, colorimetric detection methods have attracted significant attention due to their low cost, operational simplicity, and ability to provide visual results without specialized equipment [13-18]. Besides, smartphones show enormous potential for digital color examination of real samples on-site detection, owing to their portability and ease of use [19, 20]. Smartphones with high-resolution cameras can rapidly capture color images, while third-party applications enable simultaneous extraction and analysis of multiple color parameters, allowing for quick test results [21-23].

To overcome the sensitivity limitations inherent in conventional colorimetric methods while maintaining smartphone-based portability, researchers have investigated nanozymes as enhanced catalytic modules. Concurrently, biosensing technology based on nanozymes has made remarkable progress [24]. In particular, gold nanoparticles (AuNPs) have attracted considerable research attention owing to their unique catalytic performance [25]. Nevertheless, conventional AuNPs-based colorimetric methods suffer from inherent limitations such as monochromatic responses and limited sensitivity [26, 27]. In contrast, oxidative etching of gold nanorods (AuNRs) offers a promising solution, leveraging their anisotropic plasmonic properties [28, 29]. This approach involves controlled oxidation of AuNRs by specific oxidants, systematically reducing their aspect ratios. The consequent blue shift in the longitudinal surface plasmon resonance (LSPR) peak, accompanied by distinct color transitions, enables highly tunable and sensitive detection [30]. Owing to their enhanced LSPR tunability compared to isotropic AuNPs, AuNRs provide superior quantitative signal output capabilities [31, 32]. This methodology has been successfully implemented in various applications, including food safety monitoring, environmental pollutant detection, and clinical diagnostics [33, 34].

This study revealed the mechanism by which AGs regulate the peroxidase (POD)-like and catalase (CAT)-like activities of AuNPs. Based on this mechanism, two multicolor visual biosensors employing AuNPs as recognition elements and AuNRs as signal transduction elements were constructed to analyze KAN and TOB with smartphone respectively (Fig. 1). Under neutral conditions, KAN enhanced the POD-like activity of AuNPs, promoting the generation of higher concentrations of the etching agent TMB^{2+}. As the KAN concentration increased, the length-to-diameter ratio of AuNRs progressively decreased, resulting in a gradual blue shift of the LSPR peak. Under alkaline conditions, TOB enhanced the CAT-like activity of AuNPs, accelerating the decomposition of H_2O_2 and thereby reducing the available H_2O_2 for the etching

reaction. As the TOB concentration increased, the production of the etchant I_3^- diminished, which inhibited the reduction in the length-to-diameter ratio of AuNRs and led to a progressive red shift of the LSPR peak. The distinct colorimetric responses enabled smartphone-based on-site detection of AGs in milk samples. This study establishes a novel biosensing strategy with broad applications in food safety.

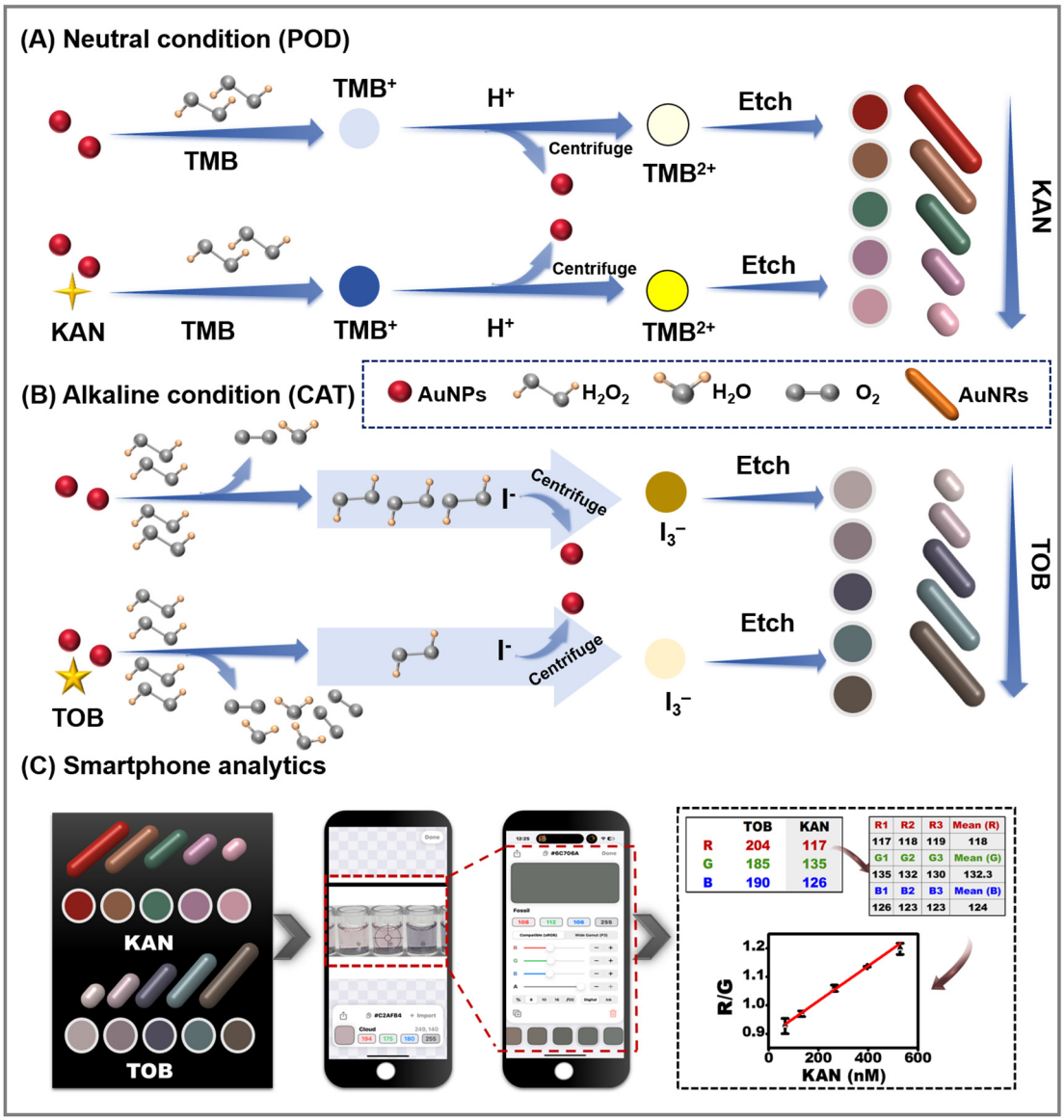

Fig. 1 Schematic illustration of detection mechanisms. (A) KAN detection via AuNPs-modulated POD-like activity under neutral conditions. (B) TOB detection via AuNPs-modulated CAT-like activity under alkaline conditions. (C) Smartphone-based detection platform.

2. Materials and methods

2.1. Materials and reagents

Silver nitrate ($AgNO_3$), cetyltrimethyl ammonium bromide (CTAB), L-ascorbic acid (AA), sodium borohydride ($NaBH_4$), Gold chloride tetrahydrate ($HAuCl_4{\cdot}4H_2O$), 3,3′,5,5′-Tetramethylbenzidine (TMB), Sodium citrate ($C_6H_5Na_3O_7$), acetic acid (HAc), sodium acetate (NaAc), and tobramycin were obtained from Sangon Biotechnology Co. Ltd. (Shanghai, China). Hydrochloric acid (HCl) and hydrogen peroxide(H_2O_2) were purchased from Beijing Chemical Works (Beijing, China). Kanamycin was obtained from Aidisheng

Biotechnology Co. Ltd. (Jiangsu, China). All reactants were used without further purification. Ultrapure water was provided by the Millipore Milli-Q system.

The transmission electron microscopy (TEM) images were recorded with a JEM-2100 transmission electron microscope (JEOL, Tokyo, Japan). The UV-vis absorption spectra were collected by a 2550 UV-vis spectrophotometer (Shimadzu, Tokyo, Japan). Zeta potential and size values were obtained by a Zetasizer Nano-ZS Nanoparticle Size Potentiometer (Malvern, U.K.). Fourier transform infrared spectra (FTIR) were obtained using an IRPrestige-21 spectrometer (Shimadzu, Japan).

2.2. Synthesis of AuNPs and AuNRs

Citrate-stabilized AuNPs (13 nm) were synthesized according to the method described in the literature [35]. The concentration of AuNPs was determined to be 5 nmol/L by UV-vis absorption spectroscopy. AuNRs were synthesized following the seed-mediated growth method reported in the literature [36], with the addition of 5-bromosalicylic acid (5-BrSA) as a chemical additive to enhance the aspect ratio. The seed solution was prepared by mixing $HAuCl_4 \cdot 4H_2O$ (50 mmol/L, 0.025 mL) and CTAB (0.1 M, 4.7 mL) with a cold $NaBH_4$ solution (0.01 M, 0.3 mL), followed by vigorous stirring at 25 ℃. The seed solution was then aged for 30 min at 30 ℃ before use. To prepare the growth solution, 0.11 g of 5-BrSA and 0.91 g of CTAB were fully dissolved in 25 mL of water, followed by $HAuCl_4 \cdot 4H_2O$ (0.001 M, 25 mL) and $AgNO_3$ (0.008 M, 0.6 mL). Subsequently, 0.2 mL of ascorbic acid solution (0.64 M) was added to the growth solution. Finally, 80 μL of seed solution was introduced, the mixture was vigorously stirred, and then incubated at 30 ℃ for 12 h. The synthesized AuNRs were purified by centrifugation at 8,500 r/min for 20 min. The resulting precipitate was collected and redispersed in 0.2 M CTAB solution for subsequent use.

2.3. Procedure of KAN and TOB detection

A 10 μL aliquot of different KAN concentrations was added to 100 μL of solution containing 30 μL of AuNPs (0.71 nmol/L), followed by incubation at 4 ℃ for 10 min. Subsequently, 50 μL of H_2O_2 (0.95 M) and 50 μL of TMB (0.12 mmol/L) were added to the mixture, which was then incubated at 4 ℃ for an additional 15 min. The reaction was terminated by adding 50 μL of HCl (0.19 M). AuNPs were removed by centrifugation at 10,000 r/min for 10 min. Then, 120 μL of the resulting supernatant was mixed with 100 μL of AuNRs solution and reacted at 30 ℃ for 10 min. After etching, the absorption spectra of the AuNRs solution were captured with a microplate reader, and the solution color was documented photographically.

Similarly, 10 μL aliquots of different TOB concentrations were added to 100 μL of NaOH solution (3.06 mmol/L) containing 30 μL AuNPs (0.94 nmol/L), followed by incubation at 25 ℃ for 10 min. Subsequently, 50 μL of H_2O_2 (50 mmol/L) was added and the mixture was incubated at 37 ℃ for 1 h. The AuNPs were then removed via centrifugation at 10,000 r/min for 10 min. Next, 100 μL of the resulting supernatant was mixed with 100 μL of 0.1 M NaAC-HAc buffer solution (pH 4.0) and 50 μL of 10 mmol/L KI solution. The mixture was incubated at 25 ℃ for 10 min, after which the reaction product was combined with 100 μL of AuNRs solution and incubated at 50 ℃ for an additional 10 min. After etching, the absorption spectra of the AuNRs solution were captured with a microplate reader, and the solution color was documented photographically.

Under standardized conditions, images were captured perpendicularly above the 96-well plate (maintaining a 20 cm vertical distance) using an IOS smartphone with an A4 white paper background in a uniformly illuminated chamber. The acquired images were then analyzed using specialized application software (Color Pro) to detect and quantify color changes for subsequent colorimetric analysis.

2.4. Pretreatment of milk

Milk samples were spiked with different concentrations of KAN or TOB to prepare standard addition samples. Sample preparation followed an established protocol [37]. The milk samples were prepared by mixing 4 mL of milk with 6 mL of water, then adding 2 mL of 10% trichloroacetic acid and 2 mL of chloroform in that order. The mixture was vortex-mixed for 1 min to ensure homogeneity. Subsequently, the mixture was subjected to ultrasonication at 20 ℃ for 15 min. To separate the precipitate from the supernatant, the sample was centrifuged at 13,000 r/min for 10 min following ultrasonication. The supernatant was carefully collected, adjusted to pH 7.0, and brought to a final volume of 15 mL with deionized water. Different concentrations of standard KAN and TOB solutions were added to the treated milk, KAN and TOB were determined separately according to the procedure in 2.3 and recoveries were calculated.

3. Results and discussion

3.1. Effects of AGs on AuNPs enzyme activity

Peroxidase (POD)-like activity modulation: Under neutral conditions, the presence of AuNPs facilitates the H_2O_2-mediated oxidation of TMB, resulting in the formation of a blue-colored oxidized derivative (TMB^+) [38]. As shown in Fig. 2A, when H_2O_2 was added to the AuNPs + TMB system, the TMB^+ characteristic absorption peak at 652 nm was produced (curve f). Upon addition of KAN, the characteristic absorption peak of the system at 652 nm was significantly enhanced (curve g), demonstrating the enhancement of POD-like activity of AuNPs by KAN. To quantify this enhancement, the reaction was terminated through HCl addition, converting TMB^+ to TMB^{2+} (λ_{max} = 450 nm) [39]. As shown in Fig. 2B, the absorbance at 450 nm exhibited a concentration-dependent increase with elevating KAN concentrations. Due to structural similarities, similar enhancement effects were observed with other AGs, including TOB, streptomycin, and spectinomycin (Fig. S1A). Steady-state kinetic analysis of KAN revealed typical Michaelis-Menten behavior for both TMB and H_2O_2 (Fig. S2). Lineweaver-Burk analysis (Table S1) demonstrated that the K_m value for H_2O_2 remained unchanged upon KAN addition, indicating unaltered binding affinity between AuNPs and H_2O_2. In contrast, the K_m for TMB increased significantly, suggesting that KAN selectively reduces the affinity of AuNPs for TMB.

Catalase (CAT)-like activity modulation: AuNPs exhibit CAT-like activity under alkaline conditions [40], catalyzing H_2O_2 decomposition into H_2O and O_2 with visible O_2 bubble formation. The residual unreacted H_2O_2 reacts with I^- to generate I_3^-, a moderate oxidizer capable of inducing longitudinal etching of AuNRs in the presence of CTAB (reactions 1-4).

$$2H_2O_2 \xrightarrow{\text{AuNPs}} 2H_2O + O_2 \uparrow \quad (1)$$

$$H_2O_2 + 2I^- + 2H^+ \rightarrow I_2 + 2H_2O \quad (2)$$

$$I_2 + I^- \rightarrow I_3^- \quad (3)$$

$$I_3^- + 2Au \rightarrow 2AuI + I^- \quad (4)$$

By enhancing the CAT-like activity of the AuNPs and monitoring the generated dissolved oxygen content using a dissolved oxygen meter, it was found that TOB accelerated the degradation of H_2O_2 (Fig. 2C), thus reducing the remaining H_2O_2 available for I_3^- production. This diminished I_3^- weakens its etching effect on AuNRs (The characterization of AuNRs was shown in Fig. S4). Consequently, increasing TOB concentrations lead to a redshift in the longitudinal surface plasmon resonance (LSPR) wavelength of AuNRs (Fig. 2D), which directly confirms the enhancement of CAT-like activity. Other AGs similarly enhanced the CAT-like activity of AuNPs (Fig. S1B). Steady-state kinetics for TOB were analyzed by monitoring H_2O_2 decomposition at 240 nm (ε_{240} = 39.4 M^{-1} cm^{-1}) [41]. Lineweaver-Burk plots and Michaelis-Menten curves are shown in Fig. S3. The K_m value of AuNPs for the substrate H_2O_2 decreased compared to that of the solution without TOB, indicating that TOB significantly enhanced the affinity between the AuNPs and the H_2O_2 (Table S2).

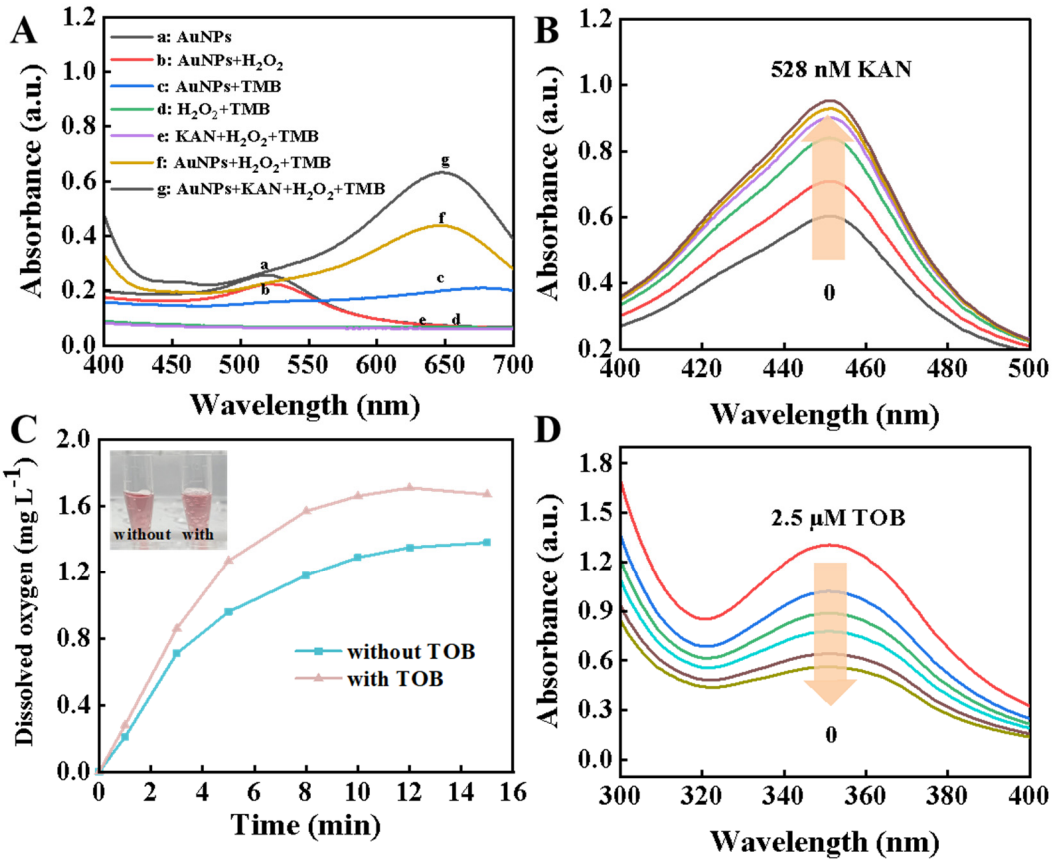

Fig. 2 (A) UV-vis absorption spectra under different reaction systems. (B) UV-vis absorption spectra after reaction termination with HCl at different concentrations of KAN. (C) The dissolved oxygen levels generated with and without TOB. (D) UV-vis absorption spectra of solutions with different concentrations of TOB.

3.2. Multicolor visual biosensor for the detection of KAN

Regulation mechanism of KAN on AuNPs POD-like activity: To elucidate the mechanism of activity enhancement, the interaction between KAN and AuNPs was initially investigated. Zeta potential measurements revealed a concentration-dependent positive shift following KAN addition (Fig. 3A),

explaining the reduced affinity between AuNPs and TMB [42]. Specifically, KAN reduced the electrostatic attraction between positively charged TMB and negatively charged AuNPs, consequently decreasing the amount of TMB adsorbed. Simultaneously, KAN induced a visible color transition from red to blue in AuNPs solutions (Fig. 3B), accompanied by a redshift of the characteristic surface plasmon resonance peak at 520 nm. TEM analysis confirmed the monodisperse spherical morphology of pristine AuNPs (average diameter: 13 nm), while KAN treatment triggered significant nanoparticle aggregation (Fig. 3C-F). These results conclusively demonstrate KAN-mediated AuNPs surface modification and subsequent aggregation.

To elucidate the adsorption mechanism of kanamycin, pH-dependent experiments were conducted. Under neutral conditions, positively charged kanamycin adsorbs onto citrate-capped AuNPs via electrostatic interactions. The color change of AuNPs was partially suppressed at pH 11 and completely inhibited at pH 12 (Fig. S5A and B). Notably, kanamycin still induced aggregation at pH 11 despite lacking a positive charge, suggesting non-electrostatic contributions. Structural analysis (Fig. S5C) identified the KAN glucopyranosyl group and the hydroxyl group on the streptavidin molecule as potential hydrogen bond donors [43]. Urea treatment (Fig. S5D) confirmed the critical role of hydrogen bonding in aggregation. Additionally, KAN's amino groups may displace weakly bound citrate ligands, further promoting aggregation [44]. These findings demonstrate that KAN drives AuNP aggregation through combined electrostatic, hydrogen bonding, and ligand displacement effects.

The catalytic mechanisms of POD-like nanozymes have been broadly classified into two categories in previous studies: hydroxyl radical generation and electron transfer processes [45]. To elucidate the catalytic mechanism of AuNPs, electron spin resonance (ESR) spectroscopy was employed to directly detect hydroxyl radicals. Using 5,5-dimethyl-1-pyrroline N-oxide (DMPO) as a spin-trapping agent, the characteristic DMPO/•OH adduct was observed, exhibiting the expected 1:2:2:1 quartet signal pattern. As shown in Fig. 3G, when AuNPs were present, which interacted with H_2O_2, the DMPO/•OH spin adducts had a more pronounced ESR signal, indicating that more hydroxyl radicals were generated during H_2O_2 decomposition. The intensity of this signal was further enhanced when KAN was added. Upon 315 nm excitation, terephthalic acid (TA) reacts with hydroxyl radicals to form 2-hydroxyterephthalic acid (TAOH), which fluoresces at 430 nm. As shown in Fig. 3H, the control system containing only TA and H_2O_2 exhibited minimal fluorescence at 430 nm, while progressive intensity enhancement was observed with increasing KAN concentrations. These results unequivocally demonstrate that KAN facilitates the generation of hydroxyl radicals.

The electron transfer capability of KAN was evaluated through cyclic voltammetry measurements comparing the electrocatalytic performance of bare and AuNPs-modified glassy carbon electrodes in the reduction of H_2O_2. As illustrated in Fig. 3I, the AuNPs-modified electrode demonstrated significant catalytic activity, while the bare electrode exhibited negligible electrochemical response. Furthermore, the strength of this signal was further bolstered when KAN was added. In conclusion, the above results indicate that the enhanced POD-like activity of AuNPs arises from two synergistic mechanisms: (1) Increased generation of

hydroxyl radicals and (2) accelerated electron transfer between AuNPs and H_2O_2. These effects compensate for the weakened affinity of TMB, thereby enhancing the POD-like activity of AuNPs by KAN.

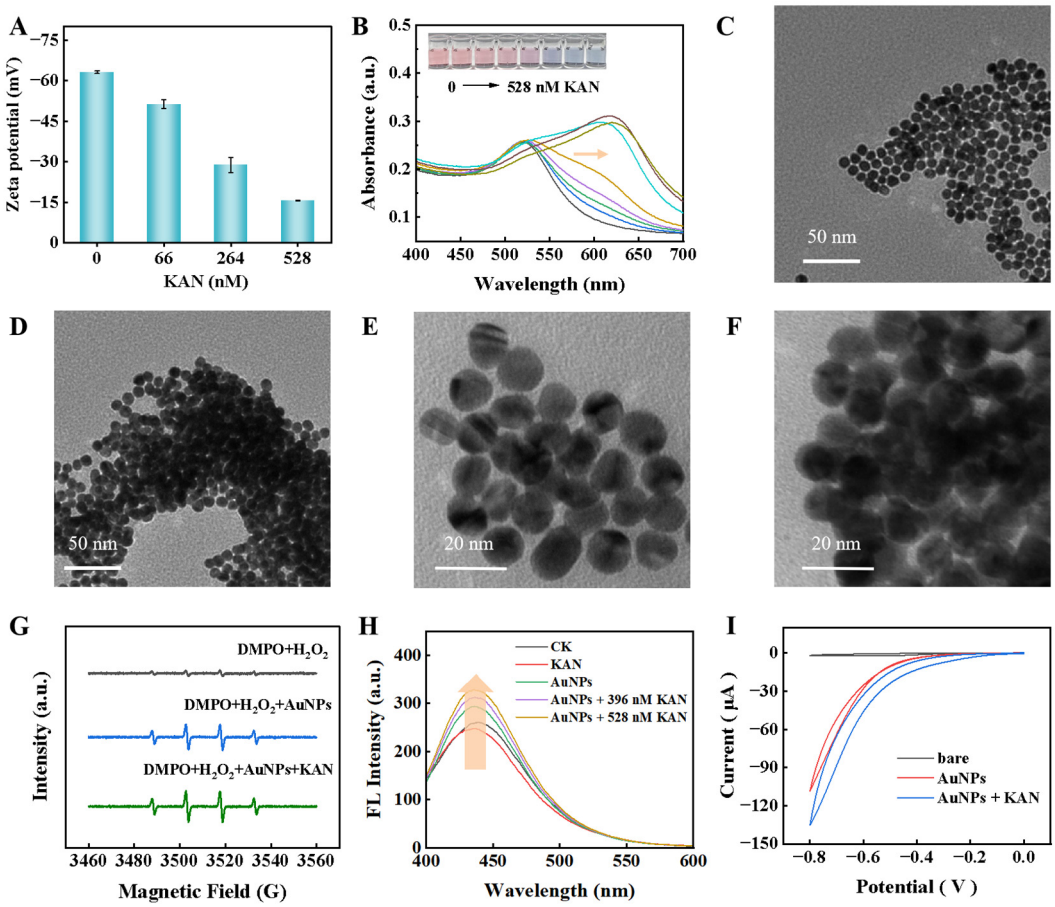

Fig. 3 (A) Zeta potential of AuNPs with different concentrations of KAN. (B) UV-vis absorption spectra of AuNPs solutions with different concentrations of KAN. (C) Low-magnification TEM images of AuNPs without KAN treatment. (D) Low-magnification TEM images of AuNPs with KAN treatment. (E) High-magnification TEM images of AuNPs without KAN treatment. (F) High-magnification TEM images of AuNPs with KAN treatment. (G) ESR signals of DMPO/•OH spin adducts in different reaction systems. (H) Fluorescence spectra for the interaction of TA with H_2O_2 in different reaction systems. (I) Cyclic voltammetry measurements comparing the electrocatalytic performance of different electrodes toward H_2O_2 reduction.

Performance detection of multicolor visual biosensor for the detection of KAN: TMB^{2+} served as the etching agent for AuNRs. To systematically investigate the concentration-dependent etching effect, TMB^{2+} stock solution (synthesized through the reaction of AuNPs with TMB and H_2O_2) was serially diluted with distilled water. Upon the addition of TMB^{2+}, UV-vis spectroscopy revealed concentration-dependent blue shifts in the longitudinal LSPR band of AuNRs (Fig. 4A). The magnitude of these LSPR shifts exhibited a positive correlation with TMB^{2+} concentration, accompanied by visually striking color changes. The sensitivity of this detection method was highly dependent on the catalytic environment and etching conditions. To enhance detection performance, the catalytic conditions were first optimized. Catalytic optimization employed the absorbance difference ($A-A_0$) at 450 nm between KAN-containing (A) and KAN-free (A_0) systems as the evaluation metric (Fig. S6). Optimal catalytic conditions were established as 15 min reaction time at 4 °C. The concentration of HCl exhibited minimal influence on the catalytic system, primarily functioning as a terminating agent that accelerates the conversion of the blue product to its yellow form without altering the overall product concentration. Consequently, the absorbance difference showed only a

marginal decrease with increasing HCl concentration. Etching condition optimization (Fig. S7) monitored the longitudinal surface plasmon resonance peak shift (Δλ) of AuNRs, identifying 0.04 M CTAB (within the optimal 0.03-0.05 M range) for controlled etching kinetics. Additional optimization determined 30 ℃ as the ideal etching temperature and 0.2 M HCl as the optimal concentration. In addition, the stability of AuNPs was evaluated. The AuNPs were extremely stable under storage conditions and maintained high peroxidase activity even at extreme pH and 80 ℃ (Fig. S8A and B), significantly outperforming natural peroxidases. Successive H_2O_2 additions demonstrated persistent catalytic activity in AuNPs, exhibiting negligible activity decay after multiple substrate additions (Fig. S8C). This confirms the exceptional operational stability and reusability of AuNPs.

Under the optimal conditions described above, quantitative analysis of KAN can be conducted based on the LSPR blue shift. The concentrations of KAN standards were quantitatively evaluated using a microplate reader based on LSPR changes within the 400 to 850 nm range, and the solution colors were documented using a camera. With the increase in KAN concentration, the LSPR of AuNRs shifted to blue (Fig. 4B). The calibration curve established a significant linear relationship with the KAN concentration in the 66-528 nmol/L range, as shown in Fig. 4C. The following was the regression equation: $\Delta\lambda = 0.096[KAN] + 2.173$. The calculated limit of detection was 3.40 nmol/L (S/N = 3), and the regression coefficient was 0.991. Comparisons with other nanozyme based KAN assays included detection range, detection limit, and reaction time (Table S3). The results showed that our system exhibited excellent performance including wider linear range, lower detection limit and acceptable detection time. To demonstrate the effectiveness of this method in detecting KAN in milk, the interference of several common substances in milk with the method was explored, including glucose (Glu), lactose (Lac), glucosamine (GlcN), N-acetylglucosamine (GlcNAc), serine (Ser), glycine (Gly), and tryptophan (Trp). The MRL concentration of 100 times KAN was used as the interferent concentration for the assay, and the results are shown in Fig. 4D. The Δλ values of the KAN-containing system were significantly higher compared to the interfering control, which confirms the immunity of the method for the detection of KAN in complex matrices. Finally, the recoveries of KAN in milk samples using the AuNPs-based colorimetric method ranged from 99.0 to 106.1% with the relative standard deviation (RSD) less than 6.7% (Table S4), which demonstrated the accuracy and precision of the method in practical applications.

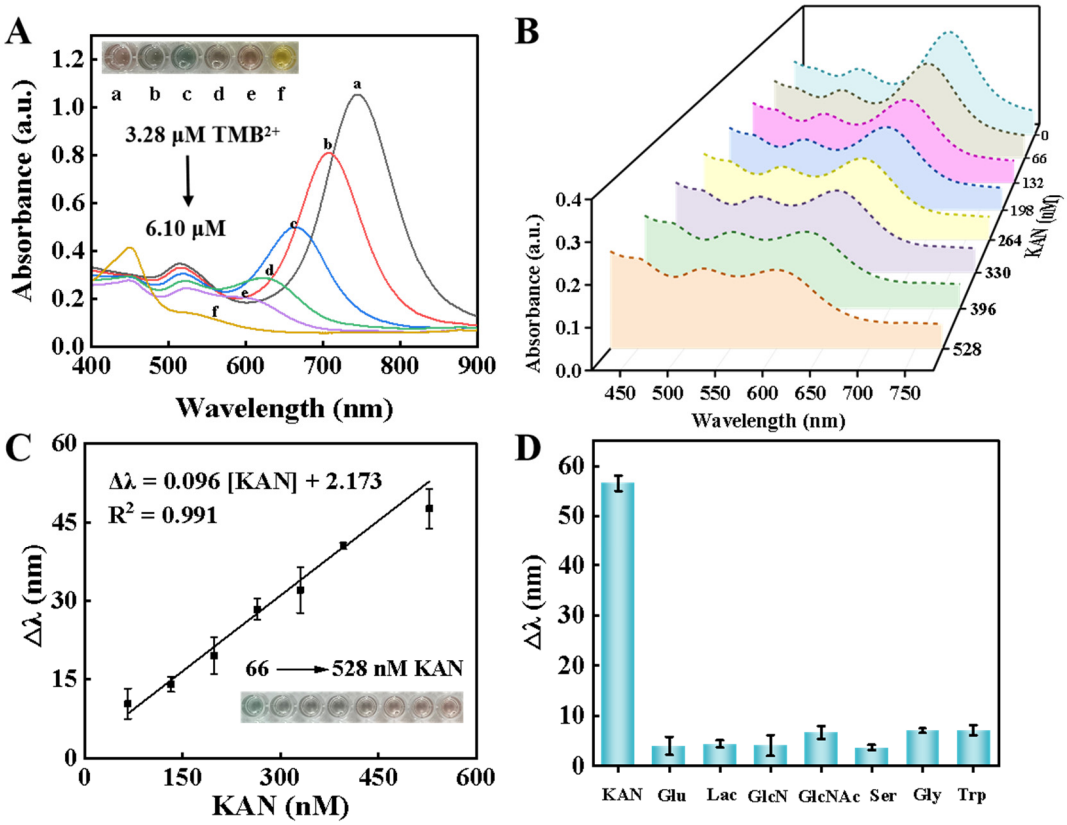

Fig. 4 (A) UV-vis absorption spectra of AuNRs after etching with different concentrations of TMB^{2+} (a: 3.28, b: 3.87, c: 4.42, d: 4.99, e: 5.58, f: 6.10 μmol/L). (B) UV-vis absorption spectra of AuNRs after etching with different concentrations of KAN. (C) Linear relationship between KAN concentration and LSPR shift. (D) Anti-interference of the sensing system toward interfering substances.

3.3. Multicolor visual biosensor for the detection of TOB

Regulation mechanism of TOB on AuNPs CAT-like activity: The mechanism underlying the enhancement of CAT-like activity in AuNPs by TOB was systematically investigated. Under experimental conditions, the aggregation of AuNPs induced by TOB was inhibited, as evidenced by zeta potential, UV-vis absorption spectra, and TEM image (Fig. 5A-C). ESR spectroscopy revealed a characteristic DMPO/•OH adduct signal in the AuNPs/H_2O_2 system (Fig. 5D), confirming the generation of hydroxyl radicals during H_2O_2 decomposition. Notably, the addition of TOB significantly attenuated this signal, suggesting that TOB suppresses the decomposition of H_2O_2 into hydroxyl radicals, resulting in a more efficient decomposition of H_2O_2 into H_2O and O_2. Subsequent monitoring of hydroxyl radical formation using a fluorescence assay with TA as a fluorescence probe corroborated that TOB itself marginally attenuated fluorescence, but in the presence of AuNPs, it induced a pronounced diminution in fluorescence (Fig. 5E). This also implied that TOB enhances the CAT-like activity of AuNPs by mitigating the decomposition of H_2O_2 into hydroxyl radicals. Cyclic voltammetry demonstrated enhanced electrochemical signals upon TOB addition (Fig. 5F), indicative of accelerated electron transfer during H_2O_2 reduction-consistent with results from Fig. 3I. The enhanced affinity between AuNPs and H_2O_2 may make it easier for the active sites of AuNPs to come into contact with H_2O_2, which would speed up the electron transfer from AuNPs to H_2O_2. Based on the above analysis, it was

shown that AuNPs enhance their CAT-like activity by curbing the production of hydroxyl radicals and accelerating the electron transfer rate in the reduction of H_2O_2.

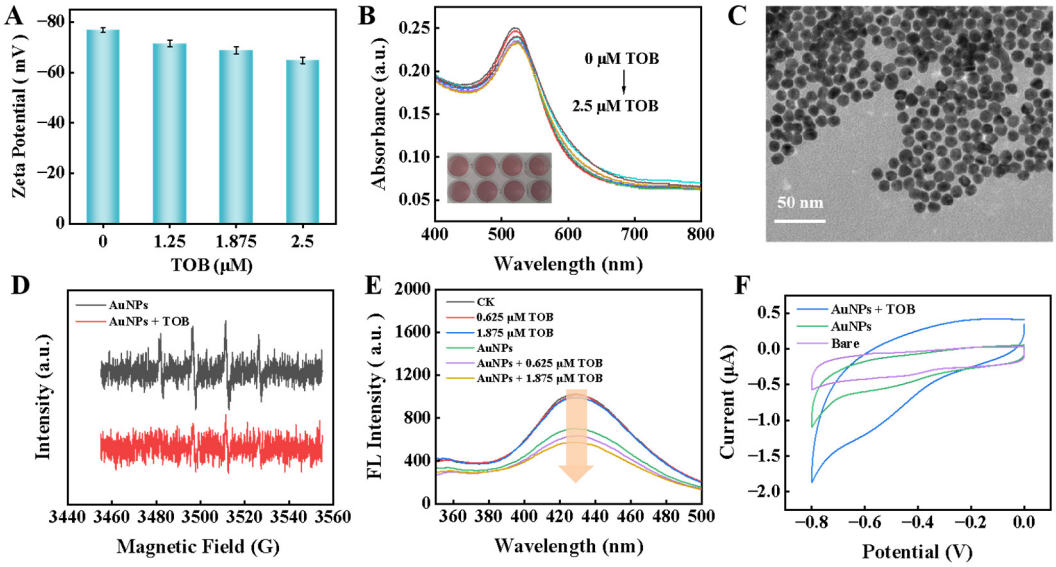

Fig. 5 (A) Zeta potential of AuNPs with different concentrations of TOB. (B) UV-vis absorption spectra of AuNPs solutions in the presence of different concentrations of TOB. (C) TEM image of AuNPs and TOB in 3.06 mmol/L NaOH solution. (D) ESR signals of DMPO/•OH spin adducts in different reaction systems. (E) Fluorescence spectra for the interaction of TA with H_2O_2 in different reaction systems. (F) Cyclic voltammograms of different electrodes.

Performance detection of multicolor visual biosensor for the detection of TOB: I_3^- served as the etching agent for AuNRs. To investigate the concentration-dependent etching effect, I_3^- stock solution was prepared by reacting H_2O_2 with I^- under acidic conditions, followed by serial dilution with distilled water. With increasing I_3^- concentration, UV-vis spectroscopy revealed significant blue shifts in the LSPR of AuNRs, accompanied by rich color changes visible to the naked eye (Fig. 6A). To enhance the sensitivity of the detection method, the catalytic conditions were optimized by monitoring the absorbance difference (A_0-A) at 350 nm. Through systematic optimization, the optimal catalytic parameters were determined as 3.06 mmol/L NaOH, 50 mmol/L H_2O_2, 37 ℃ reaction temperature, and an incubation time of 60 min (Fig. S9). Subsequently, the etching conditions were optimized by tracking the LSPR peak shift of AuNRs (Fig. S10). The results revealed that the optimal CTAB concentration was 0.04 M. Excessive CTAB likely inhibited the etching reaction due to precipitation. Further optimization identified 50 ℃ as the ideal etching temperature. Below 50 ℃, increasing the temperature accelerated the etching of AuNRs by I_3^-, whereas temperatures above 50 ℃ promoted the decomposition of I_3^- into I_2 and I^-, the former exhibiting weaker oxidative capability and thus slowing the etching rate. Finally, the optimal etching duration was determined to be 15 min.

Under these optimal conditions, the concentration of TOB standards was quantitatively assessed based on the change in LSPR over the 400-850 nm wavelength range using a microplate reader under optimal conditions (Fig. 6B). The calibration curve established a significant linear association with the TOB concentration in the 0.63-2.5 μM range, depicted in Fig. 6C. The following was the regression equation: $\Delta\lambda$ = -59.324[TOB] + 150.289. The calculated limit of detection was 0.19 μM (S/N = 3), and the regression coefficient was 0.994. Using the MRL concentration of 100 times TOB as the interferent concentration,

interference testing confirmed that the TOB assay was resistant to other components of the sample (Fig. 6D). Taking TOB in milk as an example, Table S5 indicated that the relative standard deviation (RSD) was less than 9.4%, and the recoveries ranged from 100.4% to 108.9%, which confirms its effectiveness in practical applications.

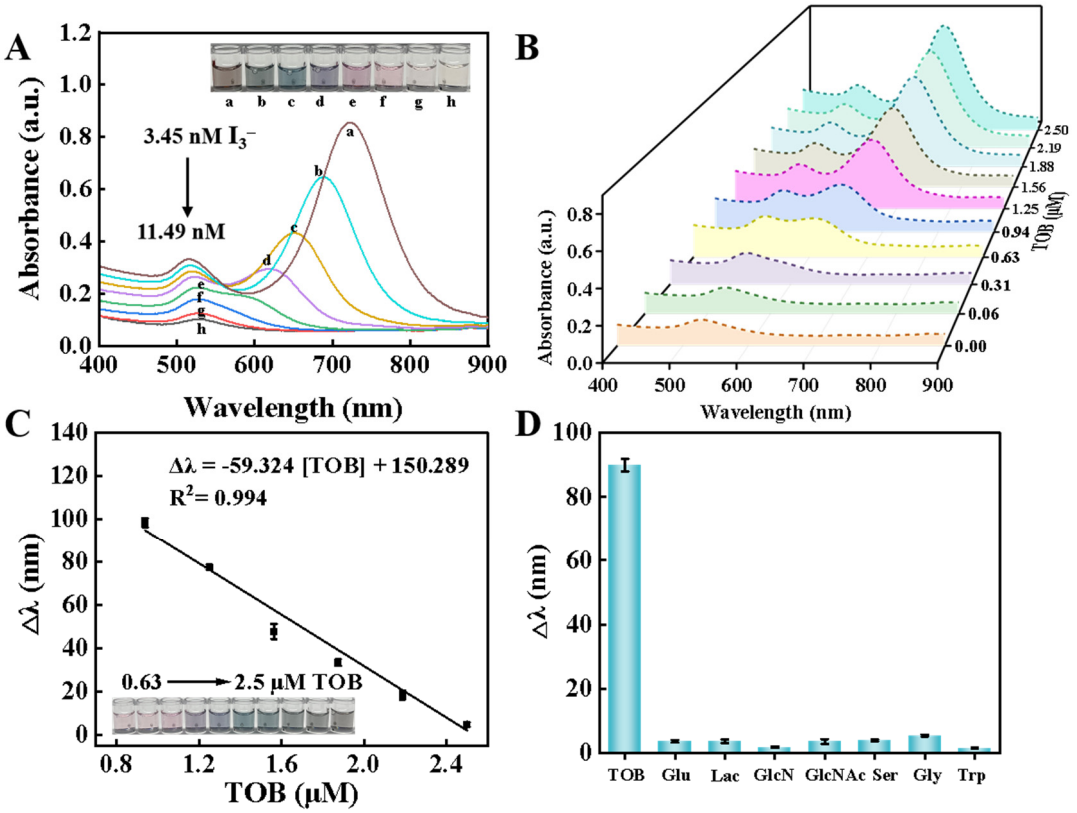

Fig. 6 (A) UV-vis spectra change of AuNRs after etching with different concentrations of I_3^- (a: 3.45, b: 4.60, c: 5.75, d: 6.90, e: 8.05, f: 9.20, g:10.34, h:11.49 nmol/L). (B) UV-vis spectra of AuNRs with different concentrations of TOB. (C) Linear relationship between TOB concentration and LSPR shift. (D) Anti-interference of the sensing system toward interfering substances.

3.4. Smartphone-based analysis of detection performance

Capitalizing on the portability and user-friendly operation of smartphone technology, we engineered a smartphone-integrated analytical platform to assess a multichannel colorimetric biosensor for antibiotic monitoring (Fig. 7A). The detection range and sensitivity of this system were rigorously validated through quantitative analysis of KAN and TOB under optimized assay conditions. As illustrated in Fig. 7B and C, KAN (0-528 nmol/L) and TOB (0-2.5 μM) were quantified by calculating the red-to-green (R/G) RGB ratio from multi-angle image captures (e.g., top-down and lateral views) using a smartphone camera paired with the "Color Pro" application. The achieved detection limits (0.28 μg/kg for KAN and 0.04 μg/kg for TOB) demonstrate exceptional sensitivity, being orders of magnitude below European Union MRLs for milk (150 μg/kg KAN; 10 μg/kg TOB). This work underscores the transformative potential of smartphone-enabled platforms in developing field-deployable biosensors.

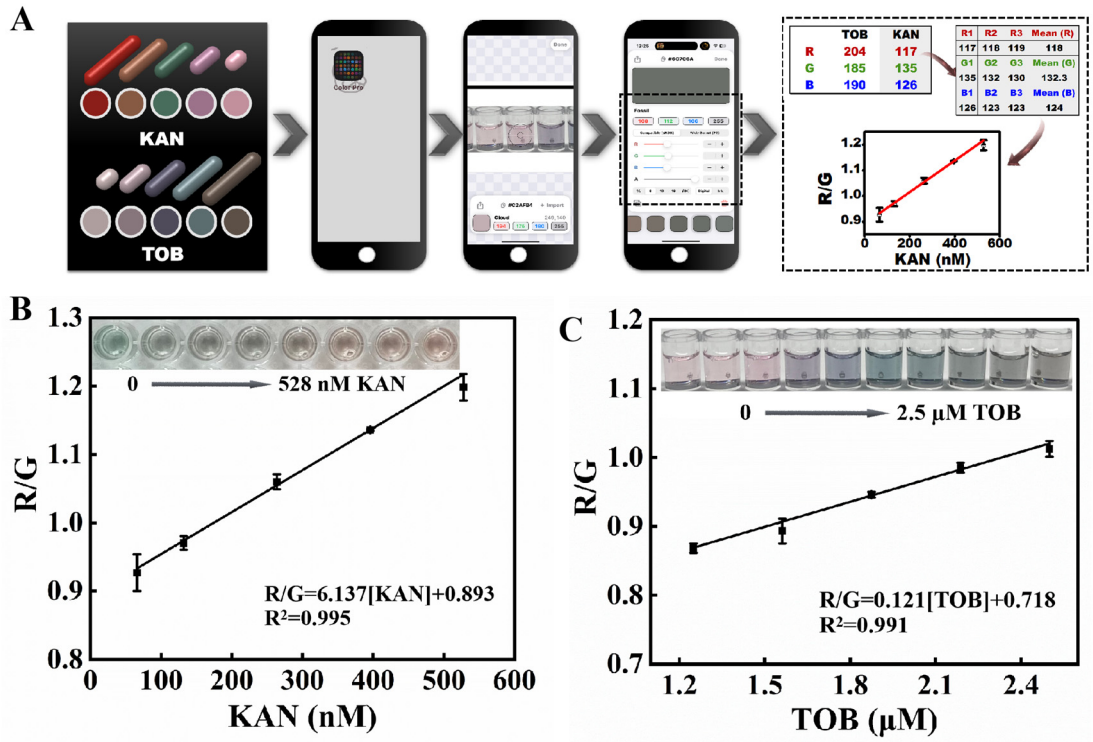

Fig. 7 (A) Schematic diagram of smartphone-based detection. (B) Photos and the linear calibration curves between smartphone-based RGB ratio values and KAN concentrations (n = 3). (C) Photos and the linear calibration curves between smartphone-based RGB ratio values and TOB concentrations (n = 3).

4. Conclusion

This study demonstrates that multienzyme-like nanozymes, exemplified by AuNPs with tunable dual POD-like and CAT-like activities, enable selective and multiplex detection of aminoglycosides through distinct catalytic pathways. KAN amplifies POD-like activity and triggers TMB^{2+}-mediated etching of AuNRs to induce LSPR blue shifts (LOD = 3.40 nmol/L), while TOB enhances CAT-like activity, suppressing H_2O_2-derived etching and generating LSPR red shifts (LOD = 0.19 μM). By replacing natural enzymes, this nanozyme-driven strategy overcomes limitations of monochromatic outputs, enabling vivid multicolor responses. Integrated with smartphone-based RGB analysis, the platform achieves on-site detection at sensitivities lower than EU regulatory limits. These results suggest the potential of multienzyme-like nanozymes in enabling adaptive biosensing platforms for food safety and environmental monitoring, especially in contexts demanding rapid, economical, and multiplexed detection capabilities. Although the sensing platform has shown excellent performance in antibiotic detection, there are still some limitations. It has only been validated for KAN and TOB, and the selection of specificity for other aminoglycosides still needs further investigation. Future research can further expand the application of this platform including the development of detection methods for other antibiotics (e.g., β-lactams, tetracyclines), and also the use of smartphone ED algorithms ($\sqrt{\Delta R^2 + \Delta G^2 + \Delta B^2}$) to obtain a superior detection limit.

Conflicts of interest

The authors declare that they have no known competing financial interests or personal relationships that could have appeared to influence the work reported in this paper.

Acknowledgement

This work was financially supported by the Science and Technology Development Program of Jilin Province, China (20220101293JC), the Natural Science Foundation of Chongqing, China (CSTB2023NSCQ-MSX0895), the Young Scientists Fund of the National Natural Science Foundation of China (62301231), National Nature Science Foundation of China (U23A20293) and the China Postdoctoral Science Foundation (2024M751092).

Appendix A. Supplementary data

The following is the Supplementary Material to this article:

Data availability

Data will be made available on request.

References

[1] Y. Tang, Y. Hu, P. Zhou, et al., Colorimetric detection of kanamycin residue in foods based on the aptamer-enhanced peroxidase-mimicking activity of layered WS_2 nanosheets, J. Agric. Food Chem. 69 (2021) 2884-2893. https://doi.org/10.1021/acs.jafc.1c00925.

[2] L. Zhu, G. Liang, C. Guo, et al., A new strategy for the development of efficient impedimetric tobramycin aptasensors with metallo-covalent organic frameworks (MCOFs), Food Chem. 366 (2022) 130575. https://doi.org/https://doi.org/10.1016/j.foodchem.2021.130575.

[3] G.M. Musiime, A.C. Seale, S.G. Moxon, et al., Risk of gentamicin toxicity in neonates treated for possible severe bacterial infection in low- and middle-income countries: Systematic Review, Trop. Med. Int. Health. 20 (2015) 1593-1606. https://doi.org/https://doi.org/10.1111/tmi.12608.

[4] Q. Zhu, L. Liu, R. Wang, et al., A split aptamer (SPA)-based sandwich-type biosensor for facile and rapid detection of streptomycin, J. Hazard. Mater. 403 (2021) 123941. https://doi.org/https://doi.org/10.1016/j.jhazmat.2020.123941.

[5] R.Y. Robati, A. Arab, M. Ramezani, et al., Aptasensors for quantitative detection of kanamycin, Biosens. Bioelectron. 82 (2016) 162-172. https://doi.org/https://doi.org/10.1016/j.bios.2016.04.011.

[6] T.M. Wassenaar, Use of antimicrobial agents in veterinary medicine and implications for human health, Crit. Rev. Microbiol. 31 (2005) 155-169. https://doi.org/10.1080/10408410591005110.

[7] Y. Xie, H. Wang, X. Yuwen, et al., Exo III-catalyzed release of a Zn^{2+}-ligation DNAzyme to drive the strand displacement reaction and gold aggregation for the homogeneous bioassay of kanamycin antibiotics, J. Agric. Food Chem. 69 (2021) 10371-10378. https://doi.org/10.1021/acs.jafc.1c04030.

[8] J.C. Paige, L. Tollefson, M.A. Miller, Health implications of residues of veterinary drugs and chemicals in animal tissues, Vet. Clin. North Am. Food Anim. Pract. 15 (1999) 31-43. https://doi.org/https://doi.org/10.1016/S0749-0720(15)30205-X.

[9] S. Yan, X. Lai, Y. Wang, et al., Label free aptasensor for ultrasensitive detection of tobramycin residue in pasteurized cow's milk based on resonance scattering spectra and nanogold catalytic amplification, Food Chem. 295 (2019) 36-41. https://doi.org/https://doi.org/10.1016/j.foodchem.2019.05.110.

[10] X. Zhou, S. Fu, J. Li, et al., Smartphone-based pH responsive 3-channel colorimetric biosensor for non-enzymatic multi-antibiotic residues, Food Chem. 429 (2023) 136953. https://doi.org/https://doi.org/10.1016/j.foodchem.2023.136953.

[11] A. Di Corcia, M. Nazzari, Liquid chromatographic–mass spectrometric methods for analyzing antibiotic and antibacterial agents in animal food products, J. Chromatogr. A. 974 (2002) 53-89. https://doi.org/https://doi.org/10.1016/S0021-9673(02)00905-6.

[12] N.C. Megoulas, M.A. Koupparis, Direct determination of kanamycin in raw materials, veterinary formulation and culture media using a novel liquid chromatography–evaporative light scattering method, Anal. Chim. Acta. 547 (2005) 64-72. https://doi.org/https://doi.org/10.1016/j.aca.2004.11.031.

[13] X. Duan, N. Zhang, Z. Li, et al., Ultrasensitive electrochemiluminescent aptasensor for trace detection of kanamycin based-on novel semi-sandwich gadolinium phthalocyanine complex and dysprosium metal-organic framework, J. Colloid Interface Sci. 632 (2023) 171-178. https://doi.org/https://doi.org/10.1016/j.jcis.2022.11.016.

[14] C.Y. Hong, X.X. Zhang, C.Y. Dai, et al., Highly sensitive detection of multiple antibiotics based on DNA tetrahedron nanostructure-functionalized magnetic beads, Anal. Chim. Acta. 1120 (2020) 50-58. https://doi.org/https://doi.org/10.1016/j.aca.2020.04.024.

[15] G. Ning, Q. Duan, H. Liang, et al., One stone two birds: electrochemical and colorimetric dual-mode biosensor based on copper peroxide/covalent organic framework nanocomposite for ultrasensentive norovirus detection, Food Sci. Hum. Wellness. 13 (2024) 920-931. https://doi.org/10.26599/fshw.2022.9250079.

[16] H. Liang, H. Liu, H. Lin, et al., Electrochemical and colorimetric dual-signal detection of Staphylococcus aureus enterotoxin B based on AuPt bimetallic nanoparticles loaded Fe-N-C single atom nanocomposite, Food Sci. Hum. Wellness. 13 (2024) 2025-2035. https://doi.org/10.26599/fshw.2022.9250168.

[17] J. Li, K. Chen, Y. Sub, et al., Paper-based biosensors based on multiple recognition modes for visual detection of microbially contaminated food, J. Fut. Foods. 4 (2024) 61-70. https://doi.org/10.1016/j.jfutfo.2023.05.007.

[18] X. Lu, B. Han, D. Wei, et al., A fluorescence-enhanced inverse opal sensing film for multi-sources detection of formaldehyde, Food Sci. Hum. Wellness. 14 (2025) 9250115. https://doi.org/10.26599/FSHW.2024.9250115.

[19] R. Jin, Z.H. Xing, D.S. Kong, et al., Sensitive colorimetric sensor for point-of-care detection of acetylcholinesterase using cobalt oxyhydroxide nanoflakes, J. Mater. Chem. B. 7 (2019) 1230-1237. https://doi.org/10.1039/c8tb02987c.

[20] X. Wei, P. Ma, K. Imran Mahmood, et al., Screening of a high-affinity aptamer for aflatoxin M1 and development of its colorimetric aptasensor, J. Agric. Food Chem. 71 (2023) 7546-7556. https://doi.org/10.1021/acs.jafc.3c01586.

[21] R. Jin, F. Wang, Q. Li, et al., Construction of multienzyme-hydrogel sensor with smartphone detector for on-site monitoring of organophosphorus pesticide, Sensor. Actuator. B Chem. 327 (2021) 128922. https://doi.org/https://doi.org/10.1016/j.snb.2020.128922.

[22] Y.Z. Shen, Y.L. Wei, X. Gao, et al., Engineering an enzymatic cascade catalytic smartphone-based sensor for onsite visual ratiometric fluorescence-colorimetric dual-mode detection of methyl mercaptan, Environ. Sci. Technol. 57 (2023) https://doi.org/10.1021/acs.est.2c07899.

[23] J. Zhang, Y. Liu, X. Cui, et al., A smartphone-integrated molecularly imprinted fluorescence sensor for visual detection of chlortetracycline based on N,P-codoped carbon dots decorated iron-based metal–organic frameworks, J. Agric. Food Chem. 71 (2023) 16303-16309. https://doi.org/10.1021/acs.jafc.3c05406.

[24] H. Cao, E. Yang, Y. Kim, et al., Biomimetic chiral nanomaterials with selective catalysis activity, Adv. Sci. 11 (2024) 2306979 https://doi.org/10.1002/advs.202306979.

[25] M. Yang, R. Wang, Y.S. Xie, et al., Applications of DNA functionalized gold nanozymes in biosensing, Biosens. Bioelectron. 271 (2025) 116987. https://doi.org/10.1016/j.bios.2024.116987.

[26] C.C. Chang, C.P. Chen, T.H. Wu, et al., Gold nanoparticle-based colorimetric strategies for chemical and biological sensing applications, Nanomaterials. 9 (2019) 861. https://doi.org/10.3390/nano9060861.

[27] J.K. Wu, L.Y. Li, D. Zhu, et al., Colorimetric assay for mercury (II) based on mercury-specific deoxyribonucleic acid-functionalized gold nanoparticles, Anal. Chim. Acta. 694 (2011) 115-119. https://doi.org/10.1016/j.aca.2011.02.045.

[28] X. Xu, X.T. Wu, Y.T. Ding, et al., Multicolorimetric sensing of histamine in fishes based on enzymatic etching of gold nanorods, Food Control. 127 (2021) 108143. https://doi.org/10.1016/j.foodcont.2021.108143.

[29] S. Wang, R. Ma, C.Q. Li, et al., Aptasensing biosynthesized phosphatidylserine with a AuNPs nanozyme-based colorimetric aptasensor, Food Sci. Hum. Wellness. 13 (2024) 823-829. https://doi.org/10.26599/fshw.2022.9250070.

[30] S.Y. Wang, Q.L. Lin, S.L. Filbrun, et al., Additive-improved colorimetric nitrite assay with ultrahigh sensitivity based on etching gold nanorods, Sensor. Actuator. B Chem. 328 (2021) 129073. https://doi.org/10.1016/j.snb.2020.129073.

[31] Y. Bao, A. Oluwafemi, Recent advances in surface modified gold nanorods and their improved sensing performance, Chem. Commun. 60 (2024) 469-481. https://doi.org/10.1039/d3cc04056a.

[32] S. Hosseinniay, A.H. Rezayan, F. Ghasemi, et al., Fabrication and evaluation of optical nanobiosensor based on localized surface plasmon resonance (LSPR) of gold nanorod for detection of CRP, Anal. Chim. Acta. 1237 (2023) 340580. https://doi.org/10.1016/j.aca.2022.340580.

[33] H. Rao, X. Xue, H. Wang, et al., Gold nanorod etching-based multicolorimetric sensors: strategies and applications, J. Mater. Chem. C. 7 (2019) 4610-4621. https://doi.org/10.1039/c9tc00757a.

[34] J.J. Li, Z.X. Zhu, M.R. Zhang, et al., Target-manipulated drawstring DNAzyme for ultrasensitive detection of UDG using Au@Ag NRs indicator, Anal. Chim. Acta. 1218 (2022) 340010. https://doi.org/10.1016/j.aca.2022.340010.

[35] G. KC, F. RG, H. MB, et al., Preparation and characterization of Au colloid monolayers, Anal. Chem. 67 (1995) 735-743. https://doi.org/10.1021/ac00100a008.

[36] X.C. Ye, L.H. Jin, H. Caglayan, et al., Improved size-tunable synthesis of monodisperse gold nanorods through the use of aromatic additives, ACS Nano. 6 (2012) 2804-2817. https://doi.org/10.1021/nn300315j.

[37]H. Ping, M.W. Zhang, H.K. Li, et al., Visual detection of melamine in raw milk by label-free silver nanoparticles, Food Control. 23 (2012) 191-197. https://doi.org/10.1016/j.foodcont.2011.07.009.

[38] Y.J. Long, Y.F. Li, Y. Liu, et al., Visual observation of the mercury-stimulated peroxidase mimetic activity of gold nanoparticles, Chem. Commun. 47 (2011) 11939-11941. https://doi.org/10.1039/c1cc14294a.

[39] X.F. Yang, W. He, Y.F. Li, et al., Telomerase activity assay via 3,3′,5,5′-tetramethylbenzidine dilation etching of gold nanorods, ACS Appl. Nano Mater. 5 (2022) 1484-1490. https://doi.org/10.1021/acsanm.1c04049.

[40] J.N. Li, W.Q. Liu, X.C. Wu, et al., Mechanism of pH-switchable peroxidase and catalase-like activities of gold, silver, platinum and palladium, Biomaterials. 48 (2015) 37-44. https://doi.org/10.1016/j.biomaterials.2015.01.012.

[41] H.Y. Sun, J. Gao, D.A. Ferrington, et al., Repair of oxidized calmodulin by methionine sulfoxide reductase restores ability to activate the plasma membrane Ca-ATPase, Biochemistry. 38 (1999) 105-112. https://doi.org/10.1021/bi981295k.

[42] L.J. Wang, H. Zhou, H.X. Hu, et al., Regulation mechanism of ssDNA aptamer in nanozymes and application of nanozyme-based aptasensors in food safety, Foods. 11 (2022) 544. https://doi.org/10.3390/foods11040544.

[43] X. Wang, M. Zou, X. Xu, et al., Determination of human urinary kanamycin in one step using urea-enhanced surface plasmon resonance light-scattering of gold nanoparticles, Anal. Bioanal. Chem. 395 (2009) 2397-2403. https://doi.org/10.1007/s00216-009-3134-9.

[44] X.L. Luo, X. Xie, Y.C. Meng, et al., Ligands dissociation induced gold nanoparticles aggregation for colorimetric Al^{3+} detection, Anal. Chim. Acta. 1087 (2019) 76-85. https://doi.org/10.1016/j.aca.2019.08.045.

[45] L.J. Zhao, J. Wang, D.D. Su, et al., The DNA controllable peroxidase mimetic activity of MoS_2 nanosheets for constructing a robust colorimetric biosensor, Nanoscale. 12 (2020) 19420-19428. https://doi.org/10.1039/d0nr05649a.